ChemComm

COMMUNICATION

View Article Online
View Journal | View Issue

Cite this: *Chem. Commun.*, 2025, **61**, 13892

Received 27th June 2025,
Accepted 4th August 2025

DOI: 10.1039/d5cc03625a

rsc.li/chemcomm

Enhancing the cycling stability of Co-free high-Ni layered cathodes through MgO surface engineering

Zi-Ting Zhou,[a] Rui-Jie Luo,[a] Chong-Yu Du,[a] Chong-Hin Tam,[a] Jie Zeng,[a] Zhe Qian,[a] Zhe Mei,[a] Yue Gu,[a] Cheng Zhang,[a] Shuang-Fu Li,[b] Ming-Xuan Yang,[b] Hang Wang,[b] Huan Ni,[b] Xiang Yin,[b] Liu Na,[b] Kai Wu[b] and Yong-Ning Zhou *[a]

A magnesium oxide (MgO) coating strategy is proposed for improving the cobalt-free high-nickel $LiNi_{0.9}Mn_{0.1}O_2$ cathode. It is revealed that a MgO coating can stabilize reversible Ni^{3+}/Ni^{4+} redox and suppress structural degradation. The MgO coated $LiNi_{0.9}Mn_{0.1}O_2$ exhibits a promising capacity retention of 66.67% after 1000 cycles at 1C rate in a wide voltage range of 2.8–4.4 V.

Lithium-ion batteries (LIBs) have dominated electric vehicle (EV) applications due to their high energy density, long cycle life and good rate capability.[1] For EV applications, $LiNi_xCo_yMn_{1-x-y}O_2$ (NCM) ternary cathode materials serve as the primary choice for high energy density LIBs. The various transition metal elements in NCM play a synergistic role in the system.[2] The rise in Ni content can increase the energy density, while adversely affecting both thermal stability and capacity retention.[3] As the Co content increases, the cation mixing and discharge capacity is reduced, with better lithium-ion transport kinetics and improved rate capability. Meanwhile, Mn serves as a structural stabilizer in the crystal lattice, which improves the material's structural stability and safety.[4] Owing to the high energy densities, high-nickel cathode materials (Ni >70%) are being widely adopted in EVs to alleviate range anxiety. Furthermore, the cost of lithium-ion batteries is largely dominated by cathode materials. Among NCM cathode components, cobalt is the most expensive element.[5] Additionally, cobalt poses environmental concerns due to its pollutive nature and the disposal processes of lithium-ion batteries.[6] Therefore, to accelerate EVs adoption, EV manufacturers seek more price-competitive adoption by lowering LIB costs. An essential step is to eliminate cobalt from cathode materials, which achieves cost reduction and improves production scalability. Cobalt's volatile price and inconsistent supply present major challenges to the sustainability of the rapidly growing EV market.[7] However, in the absence of cobalt, cobalt-free high-nickel cathodes inevitably suffer from severe interfacial side reactions, which leads to the formation of a thick and uneven cathode-electrolyte interphase (CEI) film along with increased transition metal dissolution. Consequently, these disadvantages accelerate capacity fading and cycling degradation, which significantly restricts the practical application of cobalt-free high-nickel layered cathodes.[8,9] Owing to its high capacity and low cost, the $LiNi_{0.9}Mn_{0.1}O_2$ (NM90) cathode has attracted considerable research attention, with various stabilization strategies being developed. Representative modification approaches include Mg/W co-doping for lattice optimization,[10] Nb doping for phase transition suppression,[11] and high-entropy doping strategies (Zr/Nb/Ti/Al/Mg) for microcrack prevention.[12] Additional effective approaches such as Al doping,[13] Y/W co-doping,[14] and W/Mg/Mo tri-doping have also been demonstrated to substantially improve the material's cycling stability.[15]

The capacity degradation of cobalt-free high-nickel layered oxides is primarily attributed to surface transformation rather than bulk degradation, rendering the surface engineering approach particularly critical. For instance, LiF coating has been employed to prevent direct contact between active electrode materials and electrolytes, while La_2O_3 coating enhances lithium-ion diffusion coefficients.[16,17] While these coating strategies have demonstrated certain improvements in interfacial stability, they often fail to simultaneously address multiple degradation pathways. In this contribution, we synthesize $LiNi_{0.9}Mn_{0.1}O_2$ (NM90) cathode materials *via* wet-chemical coprecipitation and implement MgO coating through sintering at 500 °C. Comprehensive structural characterization reveals that the MgO coating suppresses interfacial reactions between electrode active materials and electrolytes. Meanwhile, MgO coating reduces Li^+/Ni^{2+} cation mixing and stabilizes Ni^{3+} species to mitigate irreversible redox reactions. This work highlights the significant improvement of MgO coating in improving cycling stability and provides guidelines for developing Co-free cathode materials.

[a] *Department of Materials Science, Fudan University, Shanghai 200433, PR China. E-mail: ynzhou@fudan.edu.cn*
[b] *Contemporary Amperex Technology Co., Ningde, 352100, China*

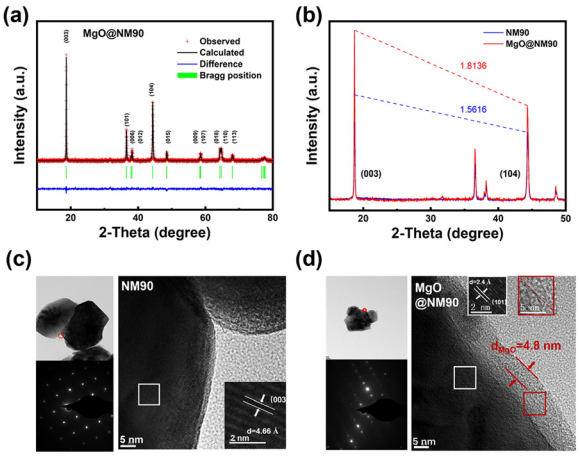

Fig. 1 (a) Rietveld refinement results of the XRD patterns of MgO@NM90. (b) The intensity ratio of the (003) diffraction peak to the (104) diffraction peak for both samples. TEM images of (c) NM90, and (d) MgO@NM90.

X-ray diffraction (XRD) patterns (Fig. 1a, b and Fig. S1, SI) show that both the pristine NM90 and coated samples exhibit sharp diffraction peaks belonging to space group $R\bar{3}m$, indicating that the as-prepared materials have good crystallinity without observable impurity phases. The diffraction peaks of the coated samples show no significant angular shifts, and no new peaks appear in the diffraction patterns, suggesting that the MgO coating did not alter the crystal structure of the NM90 material. From the intensity ratio (I_{003}/I_{104}) between the (003) and (104) diffraction planes combined with Rietveld refinement structural parameters (Table 1), it is found that the c/a value of the coated samples increases significantly, indicating that the Li^+/Ni^{2+} cation mixing ratio decreases. This is mainly attributed to the MgO coating suppressing surface side reactions and reducing the reduction process of Ni^{3+} to Ni^{2+}. Scanning electron microscopy (SEM) combined with energy dispersive X-ray spectroscopy (EDS) elemental mapping analysis (Fig. S2 and S3, SI) shows that the Mg element is uniformly distributed on the surface of the coated samples. From a fundamental morphological perspective, the average particle diameter is around 500 nm. Transmission electron microscopy (TEM) characterization (Fig. 1c and d) further confirms that both the pristine NM90 and coated MgO@NM90 samples exhibit single-crystal diffraction patterns with a hexagonal symmetry. The main body of the particles displays regular layered lattice fringes, with measured lattice fringe spacings of 4.66 and 4.84 Å, corresponding to the interplanar spacings of the (006) and (101) planes of the typical layered structure, respectively. Furthermore, TEM images of the coated samples reveal that MgO uniformly covers the particle surface with a thickness of about 4.8 nm. The coating layer does not show distinct lattice fringes, implying its amorphous structure. It helps improve the mechanical flexibility and chemical stability of the coating, making it less prone to cracking or peeling during cycling. The MgO layers effectively inhibit direct contact between the NM90 particles and electrolyte, reducing side reactions and improving the cycling stability of the material.

The charge/discharge curves (Fig. 2a) show that the charge/discharge behavior of the MgO@NM90 sample is consistent with that of the NM90 sample, indicating that the reaction pathway of the material remains unchanged after coating. However, the coated sample delivers a higher discharge specific capacity of 198.45 mAh g^{-1} at 0.1C rate (190.00 mAh g^{-1} for NM90), with a higher first-cycle coulombic efficiency of 87.77% (84.94% for NM90), which is closely related to the MgO coating suppressing surface side reactions and reducing the degree of Li^+/Ni^{2+} mixing, corresponding to the XRD refinement results. Subsequently, we performed CV tests on the materials in the voltage range of 2.8–4.4 V at a scan rate of 0.1 mV s^{-1}, as shown in Fig. 2(b). Both the NM90 and MgO@NM90 samples exhibit three pairs of reversible redox peaks, corresponding to the phase transition processes of H1–M, M–H2 and H2–H3 during lithium deintercalation, which also match well with the charge/discharge plateaus in Fig. 2(a). Additionally, the intensity of the first oxidation peak (peak A) of the coated sample is much lower than that of the pristine sample, suggesting that the H1-to-M phase transition of the layered phase is significantly suppressed. At the same time, the intensity of the third reduction peak (peak B) of the coated sample is obviously higher, indicating better phase transition reversibility and structural stability. Long-term cycling performance tests (Fig. 2c) were conducted at

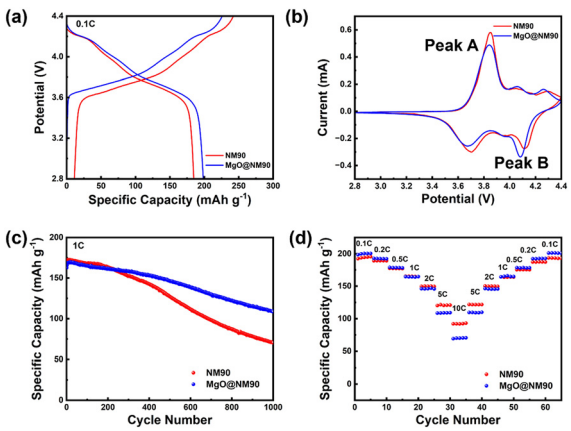

Fig. 2 (a) The initial charge and discharge curves of NM90 and MgO@NM90 at 0.1C rate (1C = 180 mAh g^{-1}). (b) CV curves of NM90 and MgO@NM90 between 2.8 and 4.4 V (scan rate: 0.1 mV s^{-1}). (c) Cycling performance of NM90 and MgO@NM90 at 1C. (d) Rate capability of the two samples from 0.1C to 10C between 2.8 and 4.4 V.

Table 1 Rietveld refinement results of the XRD patterns of NM90 and MgO@NM90

Sample	a (Å)	c (Å)	c/a	Cell volume (Å)	Li/Ni mixing (%)	χ^2	R_{wp} (%)	GOF (%)
NM90	2.8788(8)	14.2164(7)	4.9382	102.040	5.644	1.18	5.344	1.08
MgO@NM90	2.8777(2)	14.2133(4)	4.9400	101.935	4.489	1.20	3.489	1.10

1C current density in the voltage window of 2.8–4.4 V. The results show that the pristine NM90 sample exhibits similar performance to the coated sample within the first 250 cycles, but its capacity decay accelerates severely after 250 cycles. In comparison, the coated sample maintains a capacity retention of 66.67% after 1000 cycles, while the pristine sample only retains 40.46%. As shown in Fig. 2d, MgO@NM90 exhibits near 100% capacity recovery after the rate performance test (0.1C → 10C → 0.1C), demonstrating its high reversibility and robustness. Although MgO coating introduces interfacial Li^+ transport barriers that reduce the high rate performance, it enables practically relevant capacity delivery at moderate rates (0.1C–1C), allowing the material to approach its theoretical capacity limit.

We then conducted variable scan rate CV tests on the two materials in the voltage range of 2.8–4.4 V with scan rates from 0.1 to 0.7 mV s^{-1}. As the scan rate increases, the number and shape characteristics of the redox peak pairs show no significant changes, but their intensities increase uniformly with increasing scan rate. Meanwhile, the oxidation and reduction peaks shift toward higher and lower voltages, respectively, with increasing scan rate, corresponding to increased battery polarization. Comparing the data between the pristine and coated samples in Fig. 3a and b, it can be seen that the coated sample exhibits a smaller peak shift (117.6 mV) compared to NM90 (126.7 mV). The 7.2% reduction in peak shift directly evidences suppressed voltage polarization after coating. The surface diffusion coefficients were calculated from the CV curves (Fig. S4, SI). The results show that the pristine sample has a slightly higher diffusion coefficient than the coated sample, due to the presence of the coating layer. Subsequently, we performed galvanostatic intermittent titration technique (GITT) tests on the materials in the voltage range of 2.8–4.4 V at 0.2C rate. The results in Fig. 3c and d show that MgO@NM90 exhibits a higher bulk Li^+ diffusion coefficient, with an average $\log D_{Li+}$ value of −8.67 compared to −8.86 for the bare NM90. It should be noted that the enhancement in bulk ionic transport contrasts with the coating's impediment to surface Li^+ diffusion, attributable to the coating layer restricting interfacial Li^+ transport at the surface, while promoting bulk Li^+ diffusion through mitigated cation disordering.

To investigate the reasons for improved cycling stability of MgO@NM90 from a crystal structure perspective, we employed *in situ* XRD measurement to study the structural evolution of the two samples during the first charge/discharge cycle at 0.3C (Fig. S5 and S6, SI). As shown in Fig. 4a and c, with continuous lithium extraction, the (003) peak first shifts to lower angles and then moves toward higher angles. Notably, the rightward shift of the (003) peak of the MgO@NM90 sample after charging is smaller than that of the NM90 sample, indicating that its *c*-axis interlayer spacing contraction and structural collapse are less severe than those of the NM90 sample. The peak shift of the (003) plane in the coated samples is also smaller than that in the pristine samples, further proving that the unit cell contraction and collapse are effectively suppressed in the coated samples. The calculated lattice parameters *a* and *c* during the charge and discharge process are shown in Fig. 4b and d. Since the lattice parameter *a* shows small changes throughout the charging process, the surface MgO coating has little effect on the geometric structural changes of the NM90 material along the *ab* plane during Li^+ extraction. However, the lattice parameter *c* exhibits relatively large changes during charging, and in the later stage of charging, the contraction of the coated sample material along the *c*-axis direction is significantly reduced. This indicates that MgO coating can improve material stability, and reduce lattice distortion and structural collapse, thereby minimizing the accumulation of anisotropic internal stress and the generation of microcracks within the material particles, maintaining stable cycling performance of the cathode materials. In addition, NM90 exhibits more severe morphological changes than MgO@NM90 after 300 cycles (Fig. S7, SI). This further confirms the higher structural stability after coating, as well as higher stability of the CEI layer as confirmed by XPS results (Fig. S8, SI), where the uncoated sample shows increased detrimental $Li_xPO_yF_z$ species on the surface upon cycling, implying more severe side reactions with the electrolyte.

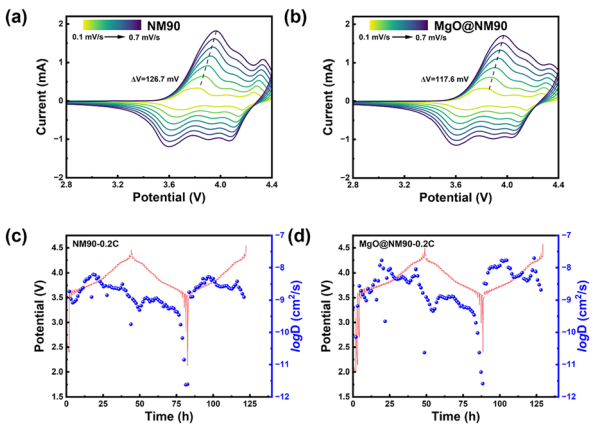

Fig. 3 Cyclic voltammogram of (a) NM90 and (b) MgO@NM90 at rates from 0.1 to 0.7 mV s^{-1}. Li^+ diffusion coefficient calculated *via* GITT of (c) NM90 and (d) MgO@NM90.

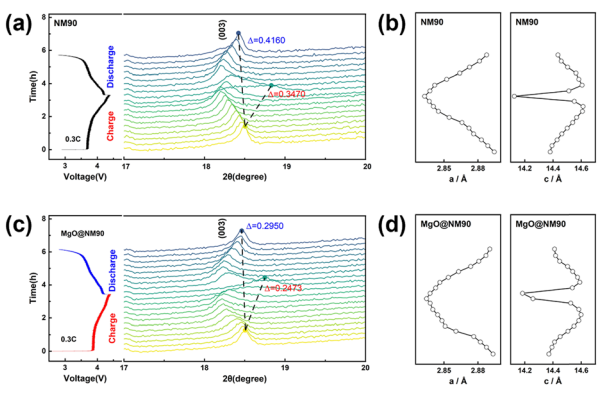

Fig. 4 *In situ* XRD (003) patterns and corresponding voltage curves during the initial cycle at 0.3C for (a) NM90 and (c) MgO@NM90. Lattice parameter evolution derived from the *in situ* XRD patterns for (b) NM90 and (d) MgO@NM90.

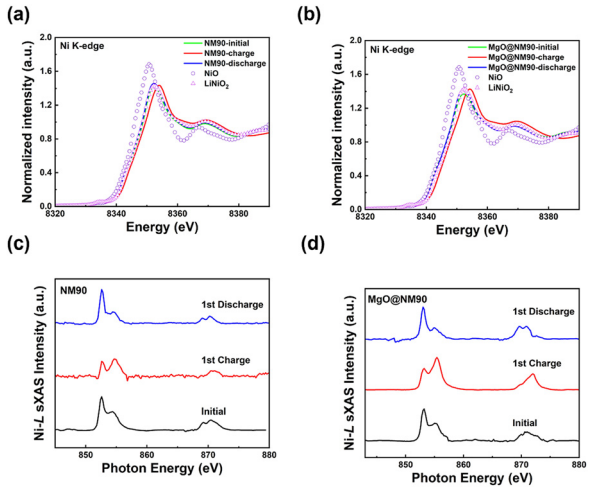

Fig. 5 Ni K-edge XAS spectra (a) and (b) and L-edge XAS spectra (c) and (d) of NM90 and MgO@NM90 at various states in the first charge and discharge processes, respectively.

To further investigate the internal effects of MgO coating on the NM90 material, we used the synchrotron radiation X-ray absorption spectroscopy (XAS) technique to characterize the changes in transition metal valence states and local structures during the first charging process. Fig. 5a and b present the K-edge XAS spectra of the Ni element in the NM90 and MgO@NM90 samples at the initial, charged and discharged states, respectively. Compared with the standard spectra of NiO and $LiNiO_2$, it can be seen that the XAS spectra of Ni in both samples at the initial and discharged states basically match the standard $LiNiO_2$, while the Ni K-edges at the charged state clearly shift toward higher energy, indicating that the valence state of Ni changes from about +3 to +4 during charging to contribute charge compensation, and returns to +3 after discharge reversibly. In comparison, the white line peak intensity of MgO@NM90 at the charged state is higher than that at the initial state, and the shift toward higher energy is more pronounced, suggesting that Ni in MgO@NM90 is more easily oxidized to higher oxidation states during charging, with more unoccupied d-orbital holes of Ni and better redox reversibility. In contrast, the white line peak intensity of NM90 at the charged state is lower than those at the initial and discharged states, indicating that Ni redox is less reversible in the uncoated sample during cycling.

Fig. 5c and d show the L-edge absorption spectra of Ni in NM90 and MgO@NM90 in total electron yield (TEY) mode, which is more sensitive to the surface. For NM90, the surface nickel primarily exists as Ni^{2+}. Upon charging, it is oxidized to Ni^{3+} and then reduced back to Ni^{2+} during discharging. It is in good agreement with the previous literature about the $LiNiO_2$ cathode.[18] For MgO@NM90, the initial surface nickel is also at Ni^{2+}. However, during charging, the nickel evolves into a mixed valence state of Ni^{3+}/Ni^{4+}, which then reverts to Ni^{2+} upon discharging. Compared to NM90, MgO@NM90 exhibits a greater proportion of nickel oxidized to higher valence states after charging, which contributes to higher capacity and demonstrates improved reversible redox behaviour.

In summary, this work reveals that MgO coating is an effective strategy to improve the electrochemical stability of the Co-free NM90 cathode for LIBs. It is found that MgO coating can suppress Li^+/Ni^{2+} mixing, stabilize reversible Ni^{3+}/Ni^{4+} redox and suppress structural degradation during cycling. In addition, MgO coating also improves the Li^+ diffusion kinetics of MgO@NM90 and suppresses interfacial side reactions. As a result, MgO@NM90 exhibits a capacity retention of 66.67% after 1000 cycles in a wide voltage window of 2.8–4.4 V at 1C rate. This work provides a promising strategy for improving the long-term cycling stability of ultrahigh-Ni layered cathode materials.

The work was financially supported by the National Key Scientific Research Project (No. 2022YFB2502300).

Conflicts of interest

There are no conflicts to declare.

Data availability

The data supporting this article have been included as part of the SI.

Detailed method and XRD, SEM, XPS analysis results involved in this work. See DOI: **https://doi.org/10.1039/d5cc03625a**.

Notes and references

1 G. Zubi, R. Dufo-López, M. Carvalho and G. Pasaoglu, *Renewable Sustainable Energy Rev.*, 2018, **89**, 292–308.
2 R. Ma, Z. Zhao, J. Fu, H. Lv, C. Li, B. Wu, D. Mu and F. Wu, *ChemElectroChem*, 2020, **7**, 2637–2642.
3 L. Wang, T. Liu, T. Wu and J. Lu, *Nature*, 2022, **611**, 61–67.
4 J. Zheng, W. H. Kan and A. Manthiram, *ACS Appl. Mater. Interfaces*, 2015, **7**, 6926–6934.
5 G. Patry, A. Romagny, S. Martinet and D. Froelich, *Energy Sci. Eng.*, 2015, **3**, 71–82.
6 R. Schmuch, R. Wagner, G. Hörpel, T. Placke and M. Winter, *Nat. Energy*, 2018, **3**, 267–278.
7 S. Lee and A. Manthiram, *ACS Energy Lett.*, 2022, **7**, 3058–3063.
8 W. Xiao, J. Wang, Z. Yi, C. Liu and C. Miao, *Rare Met.*, 2024, **43**, 3007–3018.
9 G. Zhang, X. Wen, Y. Gao, R. Zhang and Y. Huang, *Nano-Micro Lett.*, 2024, **16**, 260.
10 Y. Chen, G. Guo, Y. Yang, R. Zhu, T. Zhou and M. Gao, *J. Solid State Electrochem.*, 2025, **29**, 717–729.
11 C. Hu, J. Ma, A. Li, C. Li, C. Wang, Z. Chen, Z. Yang, J. Su and W. Zhang, *Energy Fuels*, 2023, **37**, 8005–8013.
12 S. Choi, W. Feng and Y. Xia, *ACS Appl. Energy Mater.*, 2024, **7**, 3339–3346.
13 H. Feng, Y. Leng, T. Chen, Y. Sun, C. Hai and Y. Zhou, *J. Alloys Compd.*, 2023, **960**, 170676.
14 H. Feng, Y. Xu, Y. Zhou, J. Song, J. Yang and Q. Tan, *J. Alloys Compd.*, 2024, **976**, 173043.
15 B. Zhang, H. Wen, K. Xian, N. Lu, C. Zheng, Z. Xiao, X. He, L. Ye, J. Wang, L. Ming, C. Wang and X. Ou, *Mater. Today Energy*, 2025, **48**, 101787.
16 M. Liu, G. Guo, J. Ji, R. Zhu and T. Zhou, *Ionics*, 2023, **29**, 2563–2572.
17 J. Peng, Y. Wei, B. Hu, L. Zhang, J. Huang, H. Tang, B. Huang, Y. Li, S. Chen and S. Xiao, *Ionics*, 2023, **29**, 2549–2561.
18 W.-S. Yoon, K. Y. Chung, J. McBreen, D. A. Fischer and X.-Q. Yang, *J. Power Sources*, 2006, **163**, 234–237.